# Computational Micromagnetics: Prediction of time dependent and thermal properties

Thomas Schrefl, W. Scholz, Dieter Süss, J. Fidler
Institute of Applied and Technical Physics, Vienna University of Technology,
Wiedner Hauptstraße 8-10, A-1040 Vienna, Austria

## ABSTRACT

Finite element modeling treats magnetization processes on a length scale of several nanometers and thus gives a quantitative correlation between the microstructure and the magnetic properties of ferromagnetic materials. This work presents a novel finite element / boundary element micromagnetics solver that combines a wavelet-based matrix compression technique for magnetostatic field calculations with a BDF / GMRES method for the time integration of the Gilbert equation of motion. In addition to the hysteresis properties, the numerical solution of the Gilbert equation simulations show that metastable energy minima and nonuniform magnetic states within the grains are important factors in the reversal dynamics at finite temperature.ation shows how reversed domains nucleate and expand. In an array of acicular NiFe elements the switching field varies by about 8 kA/m depending on the magnetic state of neighboring elements. The switching time of submicron magnetic elements depends on the shape of the elements. Elements with slanted ends decrease the overall reversal time, as a transverse demagnetizing field suppresses oscillations of the magnetization. Thermal activated processes can be included adding a random thermal field to the effective magnetic field. Thermally assisted reversal was studied for CoCrPtTa thin film media.

**Keywords:** Micromagnetism, Finite element method, Thermal activation

**Corresponding Author:**

Thomas Schrefl
Institute of Applied and Technical Physics
Vienna University of Technology
Wiedner Hauptstr. 8-10/137
A-1040 Vienna, Austria

phone: +43 1 58801 13729
fax: +43 1 58801 13798
email: thomas.schrefl@tuwien.ac.at

## 1. Introduction

The development and application of modern magnetic materials requires a basic understanding of the magnetization processes that determine the magnetic properties. Micromagnetics relates the microscopic distribution of the magnetization to the physical and chemical microstructure of a material. Recently, micromagnetic modeling has become an important tool to characterize the magnetic behavior of such different materials as thin film heads, recording media, patterned magnetic elements, and nanocrystalline permanent magnets. In addition to magnetic imaging, computational micromagnetics has become an important tool to investigate domain formation and magnetization reversal [1]. The finite element method provides a general framework to calculate static, dynamic, and thermal properties of magnetic materials used as permanent magnets, sensors or recording media. Micromagnetic finite element simulations are highly flexible, since it is possible to incorporate the physical microstructure and to adjust the finite element mesh according to the local magnetization [2].

The rapid progress of nanotechnology will lead to novel application of magnetic materials in spin electronic devices, magnetic sensors, and functional materials within the next years [3]. A prerequisite for the application of structured magnetic materials is the detailed knowledge of the correlation between the physical and magnetic structure of the system. The design of smart materials requires to predict the response of the system to external fields and temperature as a function of time. Magnetic sensors and magneto-mechanic devices consist of spatially distinct ferromagnetic parts. Modeling their functional behavior requires to take into account the magnetostatic interactions between the magnetic elements. This work introduces a novel method for micromagnetic simulations that combines a hybrid finite element (FE) / boundary element (BE) method with a wavelet matrix compression technique. Time integration schemes based on backward difference methods proved to be efficient for the simulation of time dependent effects, since the micromagnetic equations are stiff. This method is applied to simulate the switching dynamics of magnetic elements used in MRAM storage technology, where accurate prediction of the switching behavior is required. With increasing recording density and decreasing bit size, thermally activated magnetization reversal becomes an important issue in magnetic recording [4]. This work combines a finite element model of the media with numerical methods for stochastic differential equations, in order to solve the Langevin equation. The Langevin equation is believed to describe the random motion of the magnetization at finite temperatures. The finite element method effectively treats the granular structure of thin film recording media. Variations in the size and shape of the grains and the Cr segregation near grain boundaries can be taken into account. The magnetization within each grain may become nonuniform, as each grain is further subdivided into tetrahedral finite elements.

## 2. Micromagnetic and numerical background

Numerical micromagnetics starts from the total magnetic Gibbs free energy, $E_t$, which is the sum of the exchange energy, the magneto-crystalline anisotropy energy, the magnetostatic energy, and the Zeeman energy, and the magneto-elastic energy. The internal magnetostriction can be expressed in the same mathematical form as the uniaxial or cubic magnetocrystalline anisotropy. Therefore, magneto-elastic effects may be ingored in the derivation of the governing equations. The total energy can be written as follows [5]:

$$E_{\mathrm{t}} = \int \left[ A \sum_{i=1}^{3} \nabla \beta_i^{\,2} + f_{\mathrm{k}}(\boldsymbol{J}) - \frac{1}{2}\boldsymbol{J} \cdot \boldsymbol{H}_{\mathrm{d}} - \boldsymbol{J} \cdot \boldsymbol{H}_{\mathrm{ext}} \right] dV \ , \tag{1}$$

where $\boldsymbol{J} = (\beta_1,\beta_2,\beta_3)J_{\mathrm{s}}$ denotes the magnetic polarization.$A$ is the exchange constant and $f_{\mathrm{k}}$ is the magnetocrystalline anisotropy. $\boldsymbol{H}_{\mathrm{d}}$ and $\boldsymbol{H}_{\mathrm{ext}}$ denote the demagnetizing and the external field, respectively. The minimization of $E_{\mathrm{t}}$ provides an equilibrium distribution of the magnetic polarization. In order to resolve time dependent magnetization processes at finite temperatures, the Langevin equation [5]

$$\frac{\partial \boldsymbol{J}}{\partial t} = -|\gamma| \boldsymbol{J} \times (\boldsymbol{H}_{\mathrm{eff}} + \boldsymbol{H}_{\mathrm{th}}) + \frac{\alpha}{J_s} \boldsymbol{J} \times \frac{\partial \boldsymbol{J}}{\partial t} \tag{2}$$

has to be solved. In order to treat thermally activated processes a stochastic, thermal field, $\boldsymbol{H}_{\mathrm{th}}$, is added to the effective field, $\boldsymbol{H}_{\mathrm{eff}}$. It accounts for the interaction of the magnetic polarization with the microscopic degrees of freedom which causes the fluctuation of the magnetization distribution. The effective field, $\boldsymbol{H}_{\mathrm{eff}} = -\delta E_{\mathrm{t}}/\delta \boldsymbol{J}$, is the variational derivative of the magnetic Gibbs free energy. $\gamma$ is the gyromagnetic ratio of the free electron spin, and $\alpha$ is the dimensionless Gilbert damping constant. (2) gives the physical path of the system towards local energy minima. The first term describes of the right hand side the gyromagnetic precession under the influence of thermal perturbation. The second term is a phenomenological damping term [6]. The damping term causes the magnetization to become aligned parallel with the effective field. Thermal fluctuations cause the magnetization to from a random walk around its equilibrium position. If $\boldsymbol{H}_{\mathrm{th}}$ is zero, equation (2) reduces to the Gilbert equation [6]. Fig. 1 compares the deterministic motion and the stochastic motion at 300K for a single magnetic moment. At the time $t = 0$, the angle between the magnetic moment and the magnetocrystalline anisotropy axes was set to 45°.

The effective field $\boldsymbol{H}_{\mathrm{eff}}^{(k)}$ the node $k$ of an irregular finite element mesh may be approximated using the box scheme

$$\boldsymbol{H}_{\mathrm{eff}}^{(k)} = -\frac{1}{V_k} \frac{\partial E_{\mathrm{t}}}{\partial \boldsymbol{J}}, \tag{3}$$

where $V_k$ is the volume associated with the node $k$. The following conditions hold for the box volumes

$$\sum_k V_k = \int dV, \qquad V_k \cap V_l = 0 \ \text{ for } k \neq l. \tag{4}$$

The magnetic polarization is defined on the nodal point of the finite element mesh and is interpolated linearly within the each finite element.

The thermal field is assumed to be a Gaussian random process with the following statistical properties:

$$\langle \boldsymbol{H}_{\mathrm{th},\,i}^{(k)} \rangle = 0, \tag{5}$$

$$\langle \boldsymbol{H}_{\mathrm{th},\,i}^{(k)} \boldsymbol{H}_{\mathrm{th},\,j}^{(l)} \rangle = 2D\delta_{ij}\delta_{kl}\delta(t - t') \tag{6}$$

The average of the thermal field vanishes taken over different realizations vanishes in each direction $i$ in space. The thermal field is uncorrelated in time and space. The strength of the thermal fluctuations follow from the fluctuation-dissipation theorem:

$$D^{(k)} = \frac{\alpha k_B T}{\gamma J_s V_k} \quad , \tag{7}$$

where $k_B$ is the Boltzmann constant. The space discretization of (2) leads to a system of Langevin type equations with multiplicative noise.

At zero temperature the noise term vanishes and time integration can be performed using standard packages [7] for stiff differential equations. Tsiantos and co-workers [8] showed that the micromagnetic problem becomes considerably stiff in highly exchange coupled systems. In the stiff regime a combined BDF (backward difference formulae) / GMRES (generalized minimum residual) method was found to be faster than explicit time integration schemes like the Adams method or Runge-Kutta type methods. At finite temperature the noise term has to be taken into account.
As shown by Garcia-Palacios and Lazaro [9] the equation has to be interpreted in the sense of Stratonovic, in order to obtain the correct thermal equilibrium properties. The numerical integration of the stochastic differential equation is performed using the method of Heun. For the pure deterministic case the Heun method reduces to the standard second order Runge-Kutta method [10]. Numerical studies for simple spin systems confirmed that the Heun scheme is numerically more stable and allows larger time steps than the Euler or the Milshtein scheme [11].

In order to speed up the calculation of the demagnetizing field $\boldsymbol{H}_d$, we introduce a magnetic scalar potential, $U$, which eliminates the long range terms from (1) [12]. A hybrid finite element / boundary integral method [13] is used for computing the magnetostatic boundary value problem for $U$. This method is especially useful for the simulation of the magnetostatic interactions of distinct magnetic elements, since no mesh is required outside the magnetic particles. We split the total magnetic scalar potential into $U = U_1 + U_2$. The potential $U_1$ accounts for the divergence of magnetization within the particle and $U_2$ is required to meet the boundary conditions. The latter also carries the magnetostatic interactions between distinct magnetic particles. The potential $U_1$ is the solution of the Poisson equation with the natural boundary condition at the surface of the magnetic particle. The potential $U_2$ satisfies the Laplace equation everywhere and shows a jump at the surface of the particle. The computation of $U$ consists of three steps:

1. A standard finite element method is used to solve Poisson's equation for $U_1$.
2. The potential $U_2$ is calculated at the boundary

$$\underline{U}_2 = \mathbf{B}\,\underline{U}_1 \tag{8}$$

   where **B** is a $m$x$m$ matrix which relates the nodes at the surface to each other and $\underline{U}_1$ is the vector of the $U_1$ values at the surface nodes. The matrix B is dense and follows from the boundary element discretization of the double layer operator.
3. Once $U_2$ at the boundary has been calculated, the values of $U_2$ within the particles follow from Laplace's equations with Dirichlet boundary conditions, which again can be a solved by standard finite element technique.

A discrete wavelet transform [14] is applied to transform the matrix **B** and $\underline{U}_1$. The matrix vector product (8) can be evaluated in the wavelet bases. A sparse matrix is obtained after setting small elements of the transformed matrix to zero. Only about 10% non-zero entries remain, which significantly reduces the storage requirements and computation time for the calculation of $\underline{U}_2$.

### 3. Magnetostatic interactions of magnetic nano-elements

Magnetic nano-elements may be the basic structural units of future patterned media or magnetoelectronic devices [15]. Different magnetization reversal mechanisms occur depending on the strength and direction of the magnetostatic interaction field. The simulations predict a spread in the switching field due to magnetostatic interactions in the order of 8 kA/m for 200 nm wide, 3500 nm long and 26 nm thick NiFe elements with a center-to-center spacing of 250 nm. Fig. 2 gives the particle configuration used for the calculations. The original boundary element matrix of the system consists of $1.1 \times 10^7$ elements. After transformation and thresholding the matrix contains $1.9 \times 10^6$ non-zero entries, giving a sparsity of 83%. The demagnetization curve of the middle element was calculated for a pair of switched or unswitched neighbors. The magnetization of the neighboring elements was fixed assuming a small uniaxial anisotropy parallel to the long axis. Fig. 3 compares the numerically calculated demagnetization curves obtained with the conventional boundary element method and with wavelet based matrix compression. In configuration A, the magnetostatic interaction field of the switched neighbors stabilizes the center element. In configuration B, the interaction field of the neighbors favors the reversal of the center element. The comparison shows that the wavelet based matrix compression method provides accurate results. Numerical studies showed [16] that the error owing to matrix compression is in the range from 2 % to 5 %, for a sparsity between 80% a nd 90%. The numerical results agree well with experimental data obtained from Lorentz microscopy [17].

### 4. Switching dynamics of submicron elements

Koch and coworkers [18] investigated the switching behavior of micron-sized magnetic thin films experimentally and numerically. They observed switching times less then 500 ps. In this work, the influence of the geometric shape on the reversal dynamics was investigated. Submicron NiFe elements with an extension of 200x100x10 $nm^3$ switch well below 1 ns for an applied field of 80 kA/m, assuming a Gilbert damping constant of 0.1. The elements reverse by nonuniform rotation. Under the influence of an applied field, the magnetization starts to rotate near the ends, followed by the reversal of the center. This process only requires about 0.1 ns. In what follows, the magnetization component parallel to the field direction shows oscillations which decay within a time of 0.4 ns. The excitation of spin waves originates from the gyromagnetic precession of the magnetization around the local effective field. A much faster decay of the oscillations occurs in elements with slanted ends, where surface charges cause in transverse magnetostatic field. Fig. 4 which compares the time evolution of the magnetization for NiFe elements with rounded and slanted ends clearly shows the effect of the element symmetry on magnetization reversal. To further analyze this ringing phenomena Fig. 5 gives the Zeeman energy, the exchange energy, and the magnetostatic energy as a function of time. The plots show that an energy transfer occurs from magnetostatic energy to the exchange and Zeeman energy and vice versa. During the initial rotation of the magnetization, magnetic surface charges at the edges drastically increase the magnetostatic energy. In what follows, a nonuniform state which reduces the magnetostatic energy is formed. The magnetization changes periodically between a highly nonuniform magnetic states with low magnetostatic but high exchange energy and a magnetic state with high magnetostatic

energy. In addition, Fig. 5 presents a snapshot of the magnetization configuration during this process.

## 5. Thermal processes in thin film media

Finite element based micromagnetics is applied to study thermally assisted switching of thin film media in the high speed regime. Fig. 6 shows the finite element model of the grain structure. The magnetization within each grain may become nonuniform, as each grain is further subdivided into tetrahedral finite elements. The film thickness is 20 nm. The magnetocrystalline anisotropy axes are randomly oriented in-plane. The width of the Cr-enriched region near the grain boundaries is about 2 nm. In addition, Fig. 6 gives the demagnetization curves obtained from deterministic calculations. The step at an external field of $H_{ext} = -250$ kA/m indicates a metastable magnetization configuration which has to be passed during magnetization reversal.

In the numerical experiments the following procedure was applied. First the sample was saturated under the influence of an applied field of three times the anisotropy field. Then the field was reduced to zero and the remanent state was calculated. Both calculations where performed neglecting thermal fluctuations. The resulting magnetization configuration was used as initial state to calculate the thermal equilibrium state at 300 K for zero applied field using Langevin dynamics. Then a reversed field was instantaneously applied to the thermal equilibrium state, in order to simulate magnetization reversal at finite temperatures. The intrinsic magnetic properties ($J_s = 0.43$ T, $K_u = 2.2 \times 10^5$ J/m$^3$) where taken from [19]. The exchange constants where adjusted to $A = 10^{-11}$ J/m and $A^* = 0.6 \times 10^{-11}$ J/m, in order to obtain a coercive field of about 255 kA/m at 300 K. $A$ and $A^*$ denote the intragrain and intergrain exchange constants, respectively. The simulations of magnetization reversal were repeated several times, taking into account the stochastic nature of the process. The magnetization switches in less than 1 ns in about 80% of the calculations. However, reversal times up to 20 ns and higher are observed for about 20% of the realizations. Fig. 7 which gives the probability of not switching shows that the fraction of systems which remain unswitched after 1 ns decreases with increasing reversed field. The applied field is about 70% of the deterministic coercive field.

The system switches from the high remanent state to a meta-stable state where it may remain trapped for several nanoseconds. Fig. 8 gives the magnetization distribution in the remanent state, **r**, and in the metastable state, **m**. In the metastable state the bottom left grain has changed its magnetization direction. For further visualization of the stochastic reversal process, we plot the difference between the current magnetic state and the remanent state, **r**, as illustrated in Fig. 8. The grey scale maps the difference between the remanent state, **r**, and the meta-stable state, **m**. Fig. 9 compares the time evolution of the magnetization patterns for two different realizations of the stochastic process. The system either switches rapidly, forming a channel of reversed magnetization (A). Or the magnetization oscillates around the metastable state (B). After the partial reversal of the center grain, the system turns back to a state close to the original metastable state. This process is repeated several times, as the oscillations are triggered by thermal fluctuations. Eventually the system may escape from the metastable state, leading to a complete reversal. The results clearly show that metastable energy minima and nonuniform magnetic states within the grains are important factors in the reversal dynamics at finite temperature.

## 6. Summary

The results of micromagnetic finite element calculations enable the visualization of complex magnetization phenomena. Thus modeling provides a better understanding of fast switching dynamics at finite temperatures. The application of state of the art numerical techniques for the solution of the partial differential equations considerably reduces computation time.

## Acknowledgements

This work was supported by the Austrian Science Fund (Y-132 PHY). The authors thank V. Tsiantos, U. Nowak, and D. Hinzke for helpful discussions and J. Chapman and K. Kirk for providing experimental data.

## References

[1] E. D. Dahlberg and J. G. Zhu, Physics Today 48 (1995) 34.
[2] T. Schrefl, J. Magn. Magn. Mater. 207 (1999) 45.
[3] M. Johnson, IEEE Spectrum, February 2000, 33.
[4] D. Weller and A. Moser, IEEE Trans. Magn. 35 (1999) 4423.
[5] W. F. Brown Jr., Micromagnetics, Wiley, New York, 1963.
[6] T. L. Gilbert, Phys. Rev. 100 (1955) 1243.
[7] A. C. Hindmarsh, L. R. Petzold, Computers in Physics 9 (1995) 148.
[8] V. D. Tsiantos, J. J. Miles, and B. K. Middleton, in Proc. 3rd European Conference on Numerical Mathematics and Advanced Applications, Enumath 99 (World Scientific).
[9] L. Garcia-Palacios and F. J. Lazaro, Phys. Rev. B 58 (1998) 14937.
[10] P. E. Kloeden and E. Platen, Numerical Solution of Stochastic Differential Equations. Berlin, Heidelberg: Springer, 1995.
[11] W. Scholz, Diploma Thesis, Vienna University of Technology, 1999.
[12] P. Asselin and A. A. Thiele, IEEE Trans. Magn. 22 (1986) 1876.
[13] D. R. Fredkin, T. R. Koehler, IEEE Trans. Magn. 26 (1990) 415.
[14] W. H. Press, S. A. Teukolsky, W. T. Vetterling, B. P. Flannery, Numerical recipes in Fortran 77: The art of scientific computing, Cambridge University Press, 1992.
[15] S. Y. Chou, Proceedings of the IEEE 85 (1997) 652.
[16] T. Schrefl, D. Suss, J. Fidler, Proceedings of the MSM 2000, San Diego, March 2000.
[17] K. J. Kirk, J. N. Chapman and C. D. W. Wilkinson, J. Appl. Phys. Lett. 71 (1997) 539.
[18] R. H. Koch, J. G. Deak, D. W. Abraham, P. L. Trouilloud, R. A. Altman, Y. Lu, W. J. Gallagher, R. E. Scheuerlein, K. P. Roche, and S. S. P. Parkin, Physical Review Letters 81 (1998) 4512.
[19] E. N. Abarra I. Okamoto T. Suzuki, J. Appl. Phys. 85 (1999) 5015.

**Figure captions**

Fig. 1. Path of the magnetization vector towards equilibrium for a small Co sphere. Gyromagnetic precession dominates the motion for a damping parameter of $\alpha = 0.01$. Left: Deterministic motion neglecting thermal fluctions; right: Random walk at 300 K.

Fig. 2. Array of NiFe nanoelements for the simulation of magnetostatic inteactions, using the boundary element method (solid line) and wavelet based matrix compression (dashed line).

Fig. 3. Numerically calculated demagnetization curves of the center element for a pair of switched (A) and unswichted (B) neighbors. Solid lines: conventional boundary element method, dashed line: wavelet based matrix compression.

Fig. 4. Time evolution of the magnetization for a NiFe element with an extension of 200 x 100 x 10 $nm^3$. The Gilbert damping constant used in the calculations was 0.1.

Fig. 5. Micromagnetic energy contributions as a function of time the reversal of the element with rounded end. The dotted, dashed and long-dashed line give the magnetostatic, exchange, and Zeeman energy, respectively. The inset shows the magnetization distribution after 0.18ns.

Fig. 6. Left: Model of a CoCrPtTa thin film medium for the investigation of thermally activated reversal processes. Right: Demagnetization curve obtaind from solving Gilbert equation.

Fig. 7. Probability of not switching of the model system for different reversed fields.

Fig. 8. Plots of the difference from the remanent state provide a means to visualize magnetization reversal.

Fig. 9. Magnetization patterns as a function of time for two different realizations of the stochastic reversal process under the influence of a field of $H_{ext} = -255$ kA/m.

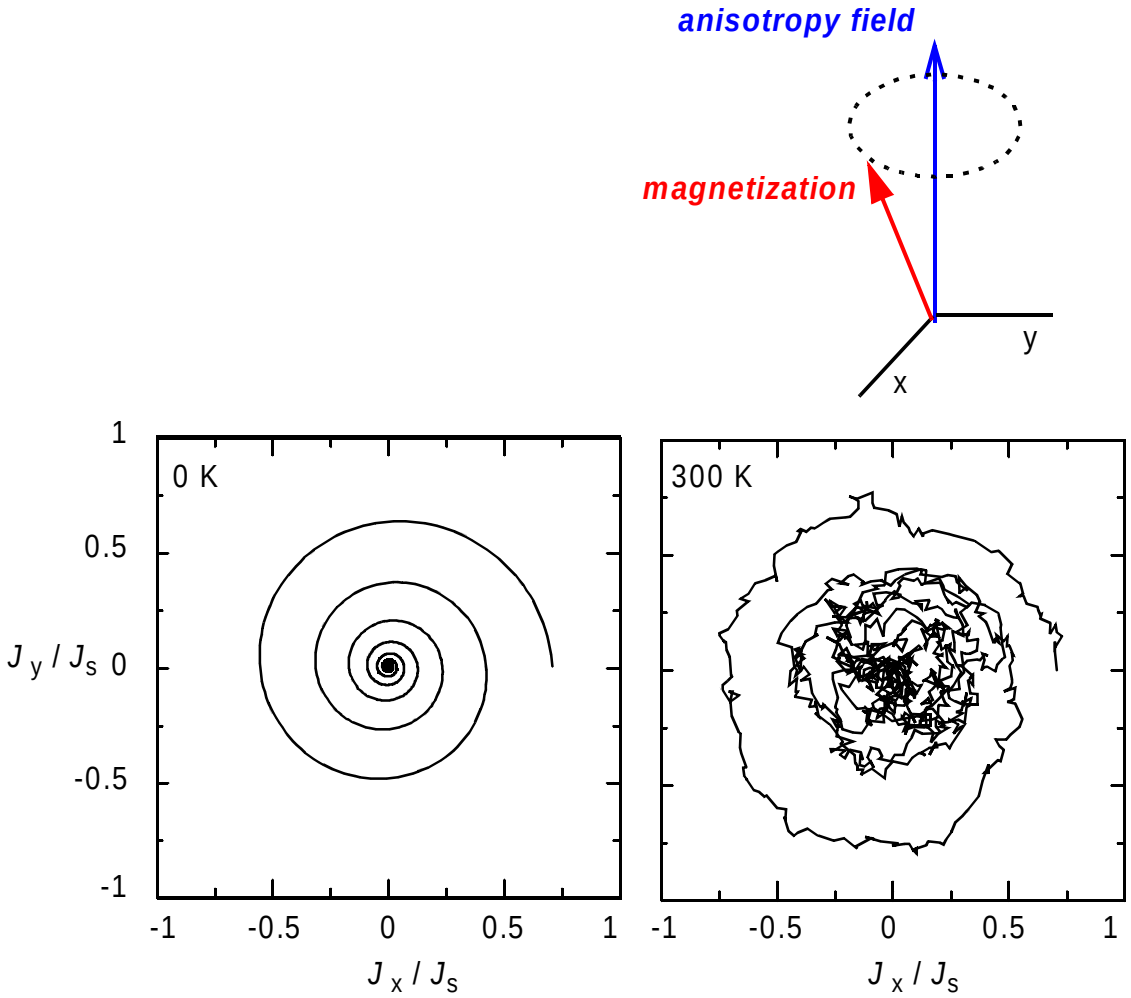
anisotropy field
magnetization
y
x
0 K
300 K
1
0.5
0
-0.5
-1
$J_y / J_S$
$J_x / J_S$
$J_x / J_S$

Figure 1

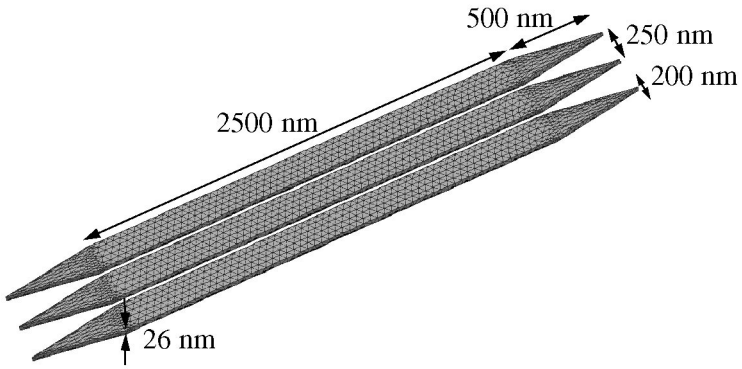


Figure 2

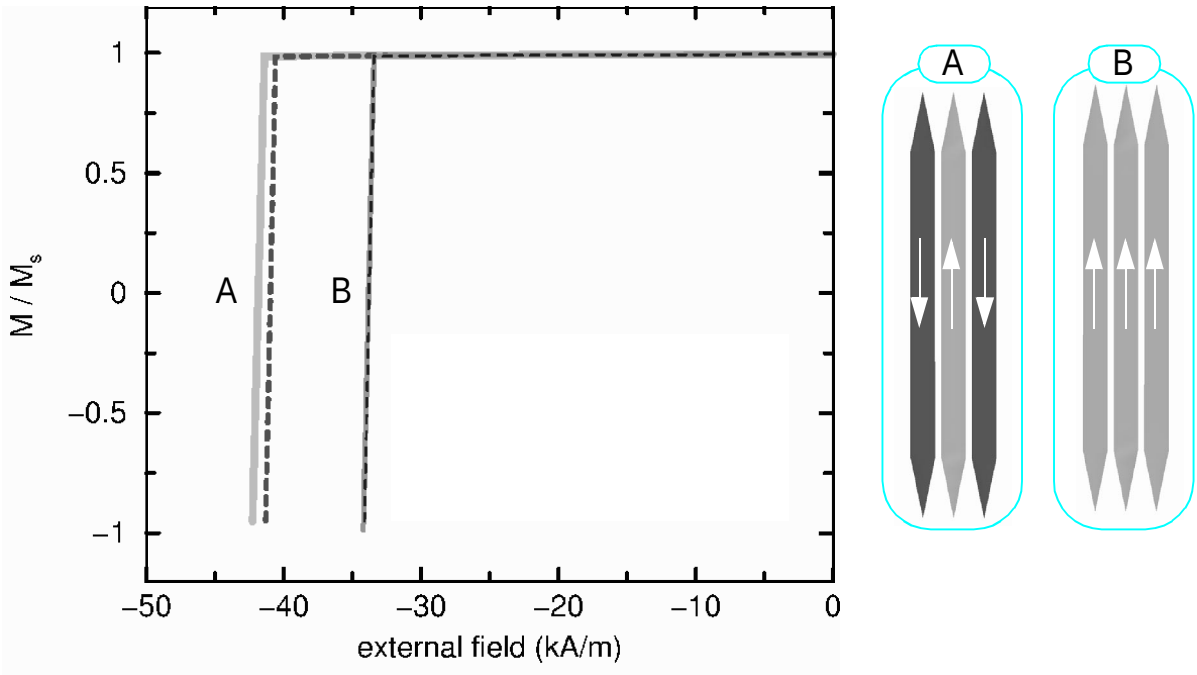


Figure 3

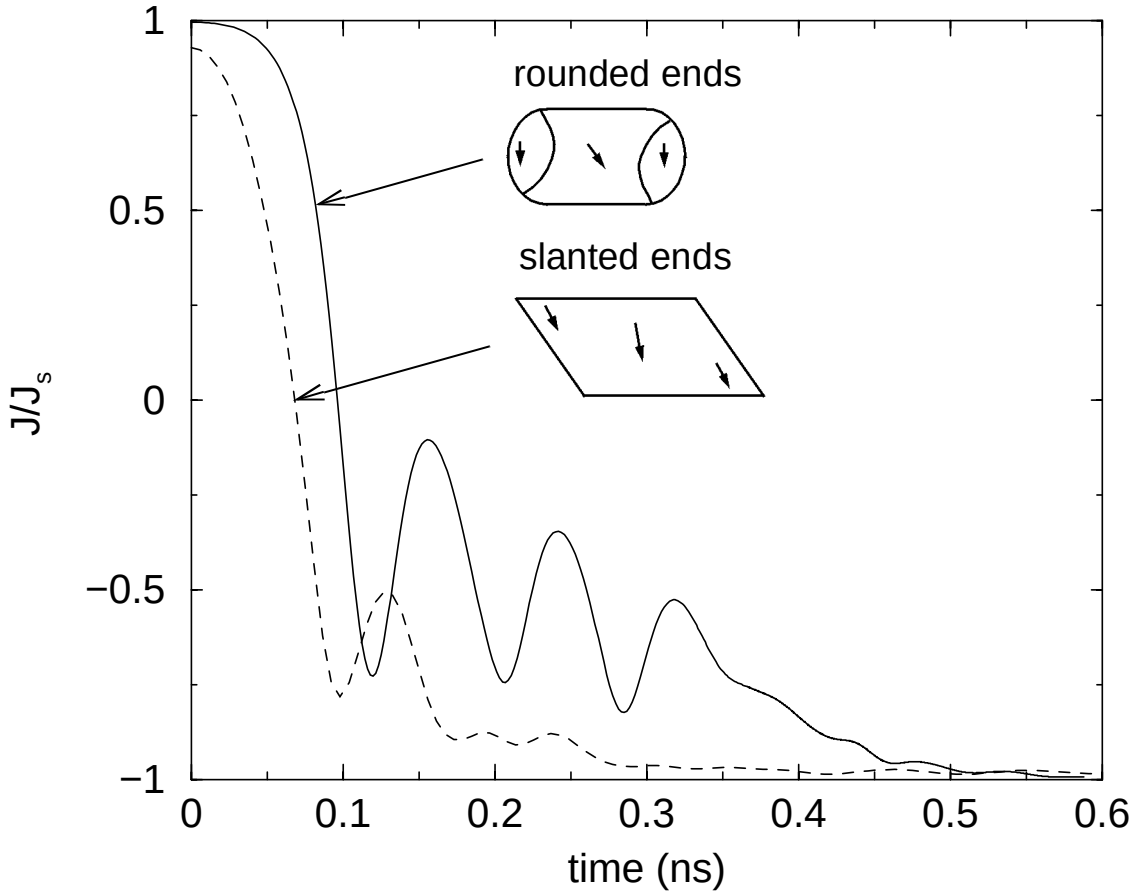
rounded ends
slanted ends
J/J_s
time (ns)
1
0.5
0
−0.5
−1
0
0.1
0.2
0.3
0.4
0.5
0.6

Figure 4

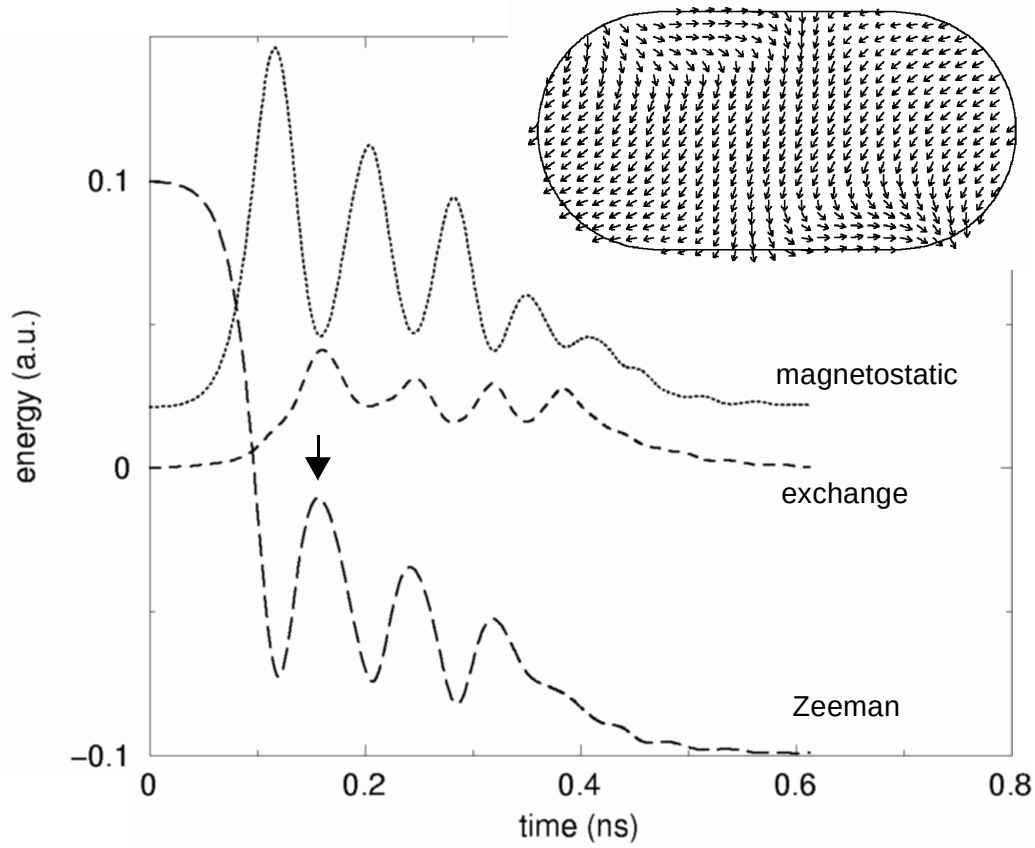


Figure 5

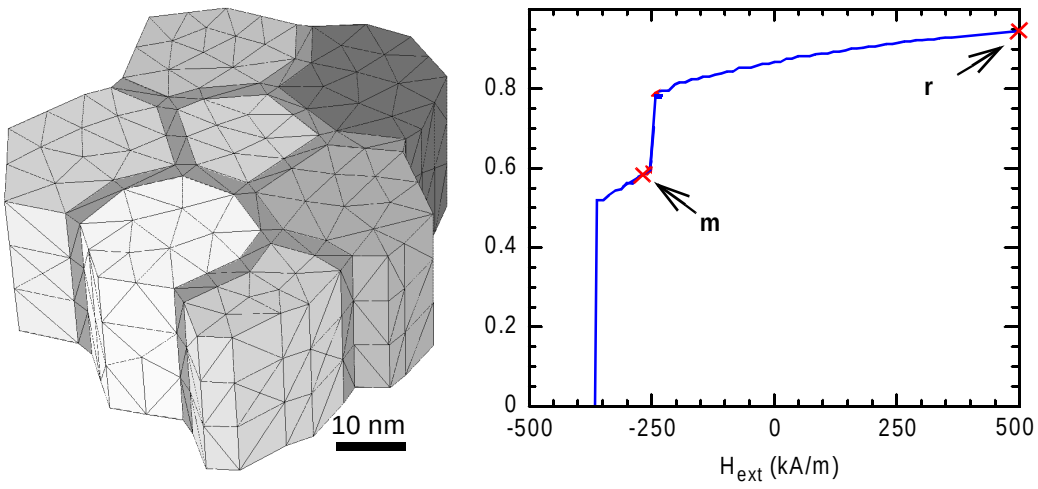


Figure 6

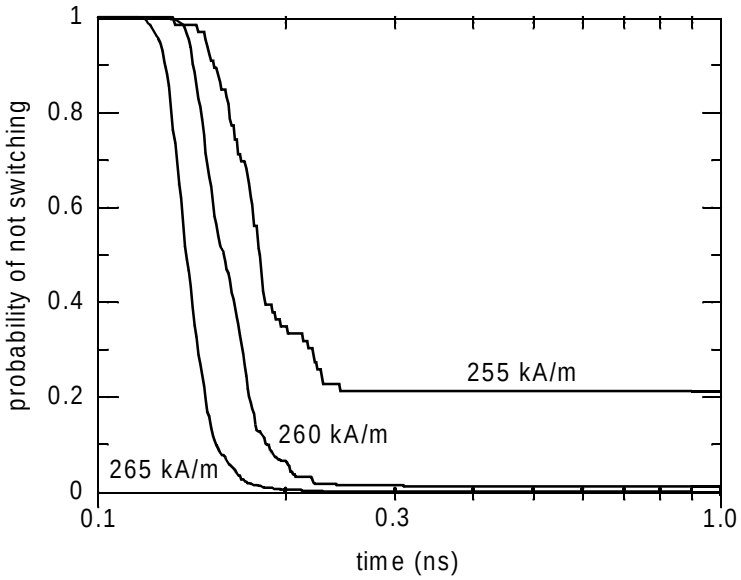
1
0.8
0.6
0.4
0.2
0
probability of not switching
0.1
0.3
1.0
time (ns)
255 kA/m
260 kA/m
265 kA/m

Figure 7

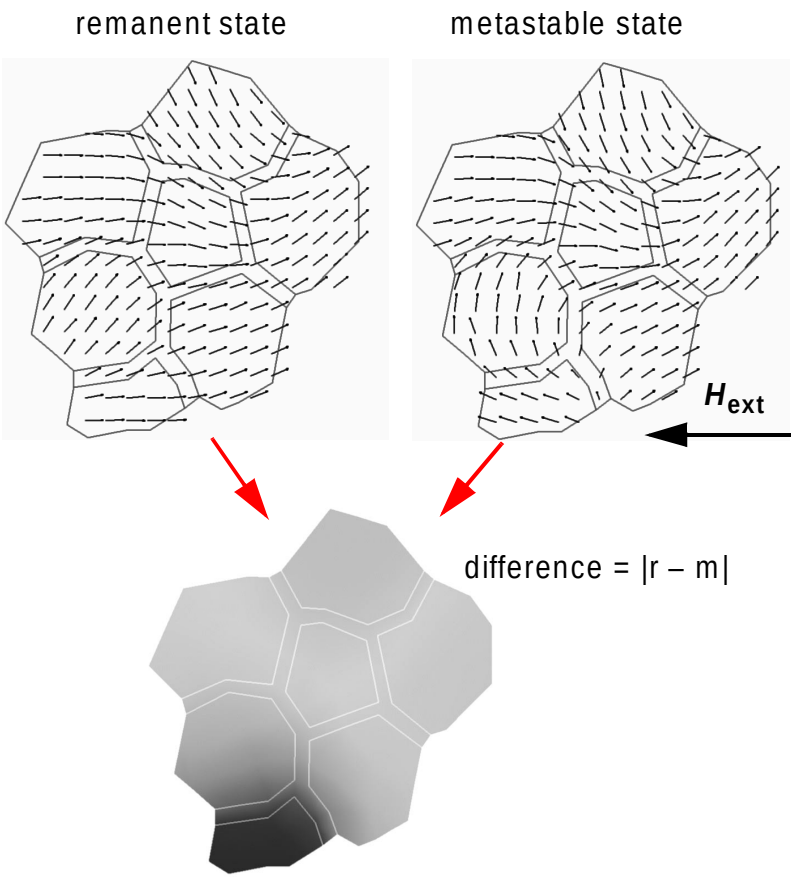


Figure 8

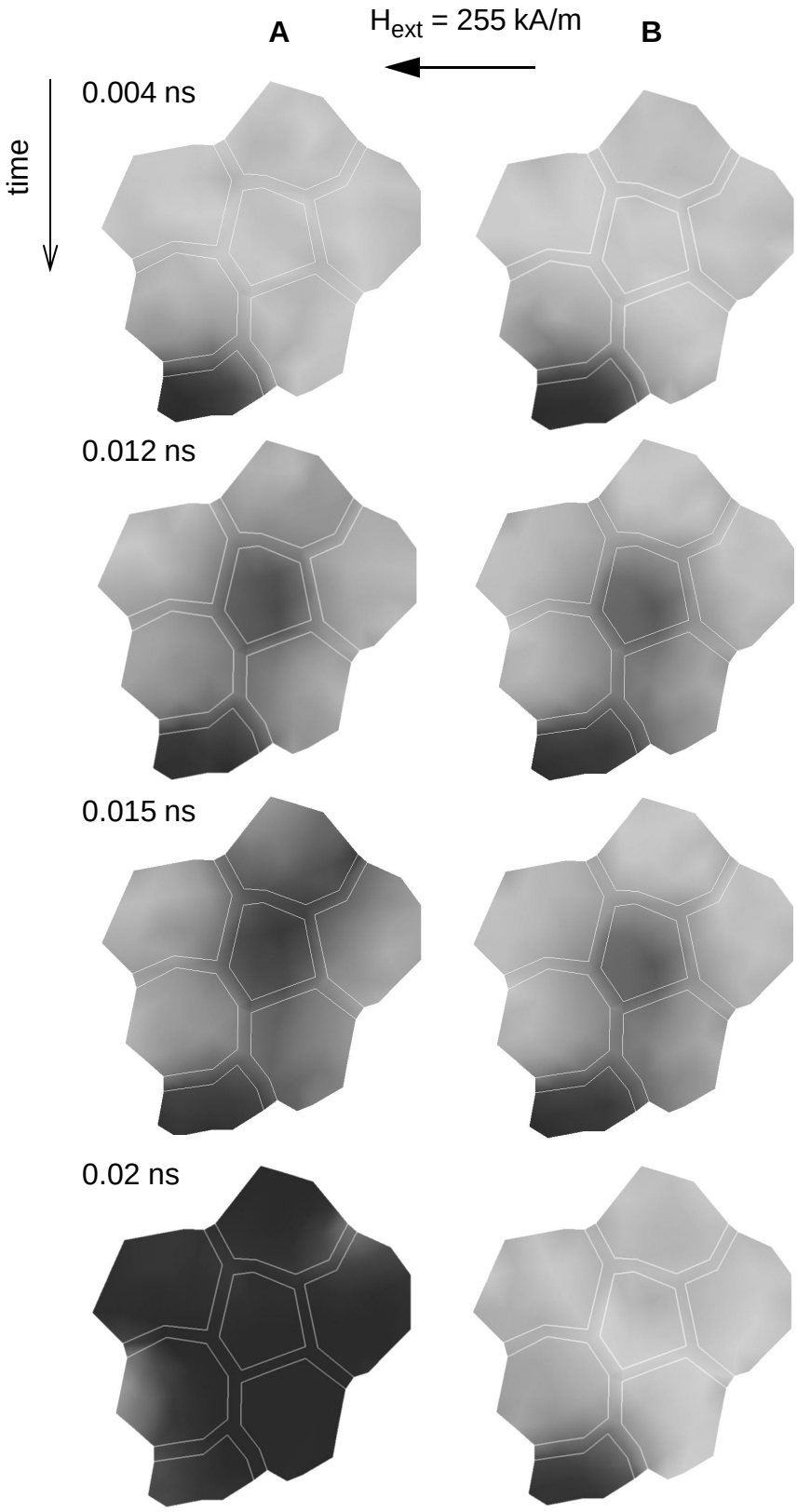


Figure 9